

## Surface diurnal cycle and boundary layer structure over Rondônia during the rainy season

Alan K. Betts,<sup>1</sup> Jose D. Fuentes,<sup>2</sup> Michael Garstang,<sup>2</sup> and John H. Ball<sup>1</sup>

Received 9 January 2001; revised 6 September 2001; accepted 11 September 2001; published 6 September 2002.

[1] An integrated data set with simultaneous observations at the surface, from tethered balloons within the boundary layer and from rawinsonde ascents, was collected during the wet season experiment of the Large-Scale Biosphere-Atmosphere (LBA) Experiment in Amazonia during January and February of 1999 in support of the ground validation for the Tropical Rainfall Measuring Mission (TRMM). We analyze the surface diurnal cycles of temperature, humidity, lifting condensation level, equivalent potential temperature, and the surface fluxes of sensible and latent heat, ground heat flux and net radiation, for easterly and westerly wind regimes in the lower troposphere. During the easterly wind regimes, the diurnal evolution of mixing ratio shows that the flux of water vapor through cloud base exceeds the large surface evaporation. There is a trend toward a wetter and cooler subcloud layer as the rainy season progresses. Daytime surface Bowen ratio for this pasture site is about 0.4, and falls slightly as the rainy season progresses. Typically in the afternoon, evaporatively driven downdrafts from convective rainbands transform the boundary layer. The fall of equivalent potential temperature in the boundary layer is similar for both regimes, but the boundary layer cooling by convective events during the westerly regimes is reduced, because the subcloud layer is shallower on average. Tethersonde ascents through the edges of gust fronts show that subcloud air is first cooled and moistened by rainfall evaporation before the arrival of downdraft air at the surface. These measurements provide a detailed observational basis for the validation and improvement of parameterizations for shallow and deep convection in numerical forecast models.

**INDEX TERMS:** 3322 Meteorology and Atmospheric Dynamics: Land/atmosphere interactions; 3374 Meteorology and Atmospheric Dynamics: Tropical meteorology; 3314 Meteorology and Atmospheric Dynamics: Convective processes; 3307 Meteorology and Atmospheric Dynamics: Boundary layer processes; **KEYWORDS:** tropical convection, diurnal cycle, boundary layer processes, surface fluxes, Amazonia

**Citation:** Betts, A. K., J. D. Fuentes, M. Garstang, and J. H. Ball, Surface diurnal cycle and boundary layer structure over Rondônia during the rainy season, *J. Geophys. Res.*, 107, 8065, doi:10.1029/2001JD000356, 2002.

### 1. Introduction

[2] During the rainy season of January and February of 1999, two campaigns were conducted in Rondônia as part of the Large-Scale Biosphere-Atmosphere Experiment in Amazonia (LBA). One was called the Wet season Atmospheric Mesoscale Campaign (WETAMC), and the second was a ground validation study for the Tropical Rainfall Measuring Mission (TRMM). The collocation at several sites of surface flux and micrometeorological instrumentation, a boundary layer tethersonde and rawinsonde system within a Doppler radar network with associated raingage networks, afforded an excellent opportunity to study the interaction of the boundary layer with convection over land in the deep tropics as well as the structure of deep convection [Cifelli *et al.*, 2002; Pereira Filho *et al.*, 2002; Silva Dias *et al.*, 2002a,

2002b]. This paper documents the key processes seen in Rondônia at one of the LBA/TRMM validation sites from the perspective of the land-surface-atmosphere interaction. This paper focuses on an observational perspective. One of our interests in LBA is to use observational analyses to improve the representation of both the land-surface, boundary layer (BL) and convective processes in global forecast models. The diurnal cycle of the BL over land in the tropics depends as much on the coupling between subcloud and cloud layers, as it does on the fluxes of sensible and latent heat at the surface-atmosphere interface. Mixing ratio and the equivalent potential temperature (or entropy) of air below cloud base are strongly regulated by the upward and downward transports by clouds, because the tropical atmosphere is nearly neutral (or even unstable) with respect to moist convection [e.g., Riehl, 1979].

[3] We will show how the diurnal cycle gives insight into these vertical transport processes by both shallow cumulus and precipitation convection, and the transition between the two, which occurs on most days near noon in Rondônia. Describing the thermodynamic and kinematic characteristics of the lower troposphere preceding, during, and after

<sup>1</sup>Atmospheric Research, Pittsford, Vermont, USA.

<sup>2</sup>Department of Environmental Sciences, University of Virginia, Charlottesville, Virginia, USA.

**Table 1.** Micrometeorological Measurements Made at the Pasture Site

Measurement	Level	Instrument
$T_{\text{soil}}$	1, 5, 20, 50 cm depth	Thermocouple
Atmospheric pressure	2 m	Pressure transducer
$T_{\text{air}}$	0.5, 1.5, 3, 6, 9.5 m	Ventilated thermistor
$T_{\text{air}}, \text{RH}$	1, 6 m	Ventilated thermistor/hygrometer
Vapor pressure, $\text{CO}_2$	0.5, 1.5, 4, 10 m	Gas analyzer (model LI-6262, LiCor)
Dew point	6 m	Chilled mirror hygrometer (General Eastern)
Wind speed, direction	10 m	Propeller anemometer (RM Young 05305)
Wind speed (u, v, w)	6 m	3-D Sonic anemometer (model K12, Gill)
Incoming solar radiation	1.5 m	Pyranometer (model PSP, Eppley)
Reflected solar radiation	1.5 m	Pyranometer (model CM3, Kipp and Zonen)
Incoming longwave radiation	1.5 m	Pyrgeometer (model CG3, Kipp and Zonen)
Outgoing longwave radiation	1.5 m	Pyrgeometer (model CG3, Kipp and Zonen)
Incoming PAR	1.5 m	Quantum sensor (model LI-190SA, LiCor)
Outgoing PAR	1.5 m	Quantum sensor (model LI-190SA, LiCor)
Soil Heat flux	5 cm depth	Plates (model 2QS, REBS)
Rainfall amount and intensity	Ground level	Tipping bucket (model TB4, Campbell Scientific)

convective storms is a key requirement to properly modeling land-surface-atmosphere interactions in global forecast modeling systems. Cloud resolving models [Tao *et al.*, 1999] are also being used to derive vertical profiles of diabatic heating to validate and confirm the heating profiles derived from the TRMM satellite. These cloud resolving models in turn need validation against data for the energy and water vapor fluxes at the surface, through the boundary layer, and through the entrainment zone. Thus, the goals of this study are to document physical processes driving the dynamics of the convective boundary layer and to derive associated composites of the thermodynamics of the system over the continental tropical atmosphere during the rainy season. In addition, it became quite clear from radar studies during the LBA/TRMM/WETAMC [Rutledge *et al.*, 2001; Rickenbach *et al.*, 2002; Peterson *et al.*, 2002], that quite distinct precipitating convective regimes existed, based on the lower tropospheric wind field. This suggests that more refined convective parameterizations may be needed, since many that are used in global models represent only a single type of parameterized convection [e.g., Betts, 1997].

[4] The results presented here go beyond previous convective experiments conducted in the Tropics. The early VIMHEX experiments in the rainy season in Venezuela in 1969 and 1972 studied the atmosphere with only a single rawinsonde, one radar, and primitive surface instrumentation [Betts, 1976a, 1976b, 1998; Betts and Silva Dias, 1979], as did similar experiments over Brazil [Silva Dias and Silva Dias, 1983]. During the Amazon Boundary Layer Experiment (ABLE-2A [Harris *et al.*, 1988]), near Manaus during the July to August 1985 dry season, the structure and growth of the mixed layer over the forest were studied using a tethered balloon and an airborne lidar [Martin *et al.*, 1988], as well as surface flux instrumentation [Fitzgarrald *et al.*, 1988]. The later dry season data from the Rondônia Boundary Layer Experiment (RBLE) showed large differences between the deep BL over grassland, where evaporation was low, and over forest where evaporation has little seasonal variability [Nobre *et al.*, 1996; G. Fisch *et al.*, Convective boundary layer over pasture and forest sites in Amazonia, submitted to *Journal of Geophysical Research*, 2001]. This study focuses on the rainy season over Rondônia at the pasture site (part of the LBA/TRMM data collection), where

complementary instruments were located to measure surface fluxes and meteorological variables, BL and atmospheric structure within a Doppler radar network.

### 1.1. Site Description

[5] Our selection and deployment of measurement systems was guided by the need to understand the link between the exchange of energy and moisture at the surface-atmosphere interface with the deeper atmosphere. The focus of our investigation was on processes that occurred on the order of seconds to hours, and on spatial scales ranging from few meters to 100 s of kilometers. The data for this study were obtained at a pasture site located near Ouro Preto d'Oeste, Rondônia, Brazil ( $10^{\circ}45'S$ ,  $62^{\circ}22'W$ ; about 30 km northwest of Ji-Paraná; see Silva Dias *et al.* [2002a]) during the wet season months of January and February 1999. The site is part of a large deforested area ( $>250 \text{ km}^2$ ) dominated by a short grass (*Brachiaria brizantha*) with isolated palm and hardwood trees scattered throughout the landscape. The landscape surrounding our measurement site is reasonably flat and situated south of the forested regions of Amazonia. The unusual experimental set-up for our investigation was the collocation of several atmospheric observing systems to study processes ranging from turbulence in the atmospheric surface layer to precipitation systems covering a wide region.

### 1.2. Measurement Systems

[6] Several complementary measurement systems were deployed and operated during January to February 1999. A 10-m flux tower was placed in the middle of the site to characterize the pasture micrometeorology; and the basic tower instruments are listed in Table 1. All measurements were acquired every 2 s, and data loggers (Campbell Scientific models 21X and CR7) produced 1-min averages. Rainfall amount and intensity were also recorded. The components of the local energy balance components were measured, including the incoming and outgoing solar and thermal energy fluxes. The soil heat flux from flux plates at 5 cm depth was extrapolated to the surface using soil temperature and a representative thermal capacity for moist soils (since soil moisture was not measured). An eddy covariance system, and a water vapor and carbon dioxide infrared gas analyzer made fast-response measurements at

10 Hz, and half-hourly turbulent fluxes of momentum, latent heat (LE), sensible heat (H), and carbon dioxide were derived.

[7] A tethered system consisting of balloon, hydraulic winch, instrumented sonde (Vaisala), and on-board data acquisition system was deployed. One complete ascending and descending profile was made every three hours at 0300, 0600, 0900, 1200, 1500, 1800, 2100, and 2400 UTC (local standard time, LST = UTC - 4). The data were logged on-board and transferred to a computer after each sounding. With a constant rate of rise and descent of  $1 \text{ m s}^{-1}$ , a 30-m<sup>3</sup> tethered balloon was used to lift a single sonde to a maximum altitude of 1500 m. The sonde was equipped with sensors to measure horizontal wind speed ( $V_s$ ) and direction, atmospheric pressure ( $p$ ), air temperature ( $T$ ), and relative humidity (RH) every 2 s, corresponding to 2 m in the vertical. Derived variables are discussed in the next section. The sonde was held at 10 m for 10 min prior to and following every ascent and descent. The purpose of the 10-m fixed level flights was to provide inter-comparison data with the 10-m level instruments on the tower. The same measurements as the tethered balloon were also made from daily rawinsonde launches at 6, 12, 15, 18, 21 and 24 UTC (which often reached the altitude of 50 km). These radiosondes (VIZ instruments) were released simultaneously with the beginning of each tethered sonde ascending flight, so that inter-comparisons between each measurement system might determine instrument offsets. Tethered balloon and rawinsonde systems provided information on the thermodynamic state of the atmosphere at discrete times. The frequency of tethered balloon and rawinsonde measurements was adequate to resolve the maximum depth of both nocturnal boundary layer and mixed daytime convective boundary layer. By colocating these two systems with the tower, the discrete vertical profiles could be compared with the continuous surface measurements, and in particular water vapor concentration measurements could be intercompared, and referenced to a gas analyzer and dew-point hygrometer.

[8] To augment airborne measurements, particularly at night, we deployed a Doppler SODAR system (model PA-1, Remtech, France) with capabilities of sounding to a nominal height of 500 m. The system was operated continuously from 20 January to 28 February 1999. The SODAR data provided turbulence statistics (standard deviation of the wind speed components:  $u$ ,  $v$ ,  $w$ , and temperature) in the lowest 500 m of the atmosphere. Also, this system provided temperature gradients and a near-continuous time and height record of mixed layer depth from 10 m to 500 m above the surface. The measurement platforms described above were in close proximity ( $\sim 3 \text{ km}$ ) of a Doppler radar system that provided information on the cloud fields and associated development of convective systems.

## 2. Derived Variables

[9] The basic thermodynamic variables we derived from measured  $p$ ,  $T$ , and RH, are potential temperature,  $\theta$ , mixing ratio,  $q$ , equivalent potential temperature,  $\theta_E$ , and the pressure height,  $P_{LCL}$ , to the lifting condensation level (LCL) or saturation pressure level,  $p^*$ . The formulae used for these are given in the table in Appendix A. The formula for saturation mixing ratio is a derivative of Wexler's formula

for saturation vapor pressure [Bolton, 1980], that for the LCL saturation temperature also come from Bolton [1980], and the formula for  $\theta_E$  comes from Betts [1982]. From the tower data, we shall use here the data measured at a height of 1.5 m for air temperature and calculate mixing ratio from the pair of temperature and relative humidity (RH) probes at 1 m. This RH data has been corrected by +3%, based on preliminary comparisons with the gas analyzer data.

### 2.1. Thermodynamic Projections

[10] We shall show plots of all four variables ( $\theta$ ,  $q$ ,  $\theta_E$ , and  $P_{LCL}$ ) against time for surface data, and subsets of them against pressure for tethered sonde and radiosonde profiles. Different thermodynamic parameters help separate different physical processes [e.g., Betts, 1984, 1992]. The daytime growing mixed layer (ML) is a layer of nearly constant  $\theta$ , above the surface superadiabatic layer, which is capped by a more stable layer, generally at cloud base in the daytime in the tropics. Mixing ratio is also nearly well mixed in this subcloud layer, although it generally falls slowly with height as drier air enters the ML from above [Betts, 1976b; Mahrt, 1976]. The level at which near-surface air becomes saturated when lifted, is close to the cloud base. We give the pressure height to this level the symbol,  $P_{LCL}$ , because, while it is computed from surface variables, it is generally an accurate daytime estimate of the depth of the subcloud layer during the morning growth phase, particularly during the rainy season when the initial predawn stable boundary layer is close to saturation.  $P_{LCL}$  is directly related to  $(1 - RH)$  by the formula [Betts, 1997]

$$P_{LCL} = p(1 - RH)/(A + (A - 1)RH) \quad (1)$$

where relative humidity as a fraction is defined as  $RH = e/e_s$  (where  $e$  is vapor pressure), and  $A = \left(\frac{\epsilon L}{2C_p T_K}\right)$ , where  $\epsilon = 0.622$  is the ratio of the gas constants for dry air and water vapor,  $L$  is the latent heat of vaporization of water,  $C_p$  is the specific heat of air at constant pressure, and  $T_K$  is the Kelvin temperature. The thermodynamic coefficient,  $A$ , increases with decreasing temperature from 2.6° at 25°C to 3.4 at -40°C.

[11] Equivalent potential temperature is an important variable for moist processes as it gives the ascent path, along a wet pseudoadiabat, for air lifted to saturation. It is conserved to good approximation in condensation and evaporative processes [e.g., Emanuel, 1994]. The surface fluxes of sensible and latent heat both increase the  $\theta_E$  of the ML, but during the daytime a near-equilibrium of  $\theta_E$  is established in the ML, because higher  $\theta_E$  is transported up into clouds, and replaced by lower  $\theta_E$  air which descends in either dry or moist downdrafts. Rain falling from clouds will evaporate in the ML, but to good approximation this does not directly change  $\theta_E$ , although it does cool and moisten the ML, and lower  $P_{LCL}$  as the air is brought closer to saturation. However, as air is cooled by the evaporation of falling rain, the negative buoyancy (which is also partly due to the weight of condensate) drives strong downdrafts which bring low  $\theta_E$  air from above down into the ML [Zipser, 1969; Betts, 1976a; Betts and Silva Dias, 1979; Garstang and Fitzjarrald, 1999].



**Table 2.** Easterly and Westerly Surface Wind Regimes

Easterly	
E1	11 Jan. 00Z–14 Jan. 00Z (DOY: 11–13)
E2	19 Jan. 00Z–29 Jan. 00Z (DOY: 19–28)
E3	8 Feb. 00Z–22 Feb. 00Z (DOY: 39–52)
Westerly	
W1	14 Jan. 00Z–19 Jan. 00Z (DOY: 14–18)
W2	29 Jan. 00Z–8 Feb. 00Z (DOY: 29–38)
W3	22 Feb. 00Z–1 Mar. 00Z (DOY: 53–59)

[12] We plot  $\theta$  against  $q$ , because slopes on a  $(\theta, q)$  plot can be thought of as Bowen ratios [Betts, 1992]. These help explain the structure of the variability of the surface variables, and the relationship of the time rate of change of the ML to the surface fluxes and entrainment fluxes. The plot of  $\theta_E$  against  $P_{LCL}$  is also useful, as it helps separate BL evaporative cooling (which reduces  $P_{LCL}$  but not  $\theta_E$ ) from the replacement of BL air by evaporatively driven down-draft air.

### 3. Surface Diurnal Cycle

[13] The variability in the surface diurnal cycle caused by synoptic processes is less marked in the deep tropics than at midlatitudes, although two distinctly different wind regimes were noted in Rondônia, dominated by surface easterly or westerly flow, as summarized in Table 2 (Day of Year is abbreviated DOY). Typically, the westerly regime was associated with a moister troposphere, and convection with weak vertical development and weak electrification, while the easterly regime had a slightly drier troposphere, stronger electrified convection with greater vertical development [Rutledge *et al.*, 2001; Cifelli *et al.*, 2002; Rickenbach *et al.*, 2002]. The larger scale associated synoptic structure of these wind regimes is explored further by Rickenbach *et al.* [2002], Silva Dias *et al.* [2002a], Peterson *et al.* [2002], and Marengo *et al.* [2002]. The westerly wind regime in Rondônia is associated with the presence of a South Atlantic Convergence Zone (SACZ), extending north-westward into Brazil, and the easterly regime with the absence of the SACZ. Herdies *et al.* [2002] discuss the bimodal nature of this summer circulation over South America.

[14] The other chief causes of heterogeneity in the day-time diurnal cycle in the rainy season are cloud cover, which reduces the incoming solar radiation at the surface, and precipitation events which sharply modify boundary layer (BL) air. We first show examples of the near surface thermodynamic diurnal cycle from three days: one from the late January easterly regime with little precipitation during most of the daytime diurnal cycle, one from the westerly regime in late February, when precipitation was more extensive and started much earlier in the day, and one from a day when a propagating convective band passed directly over the mesonet site in the afternoon. Then we show composites of the mean surface diurnal cycle from five classes: two easterly and two westerly surface wind regimes (E2, E3, W2, and W3 for which we have data at the

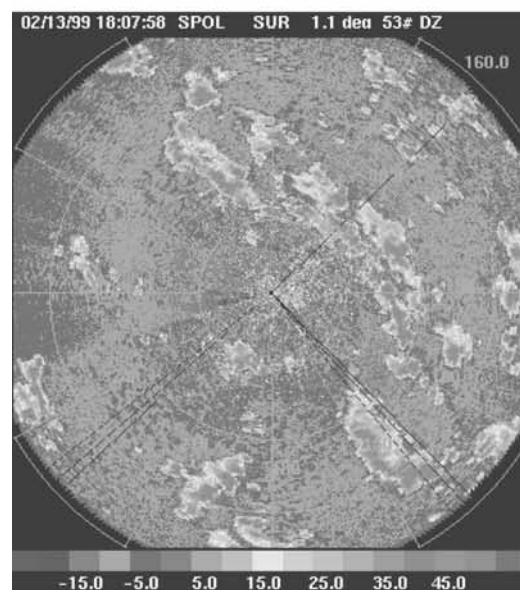
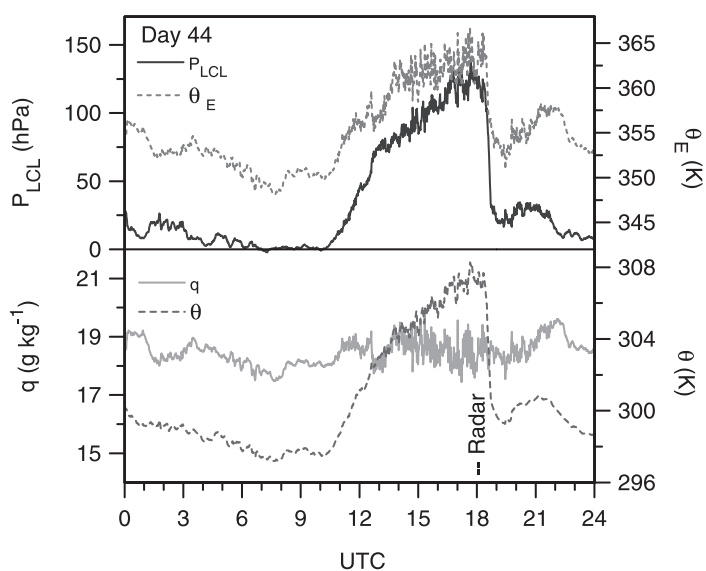
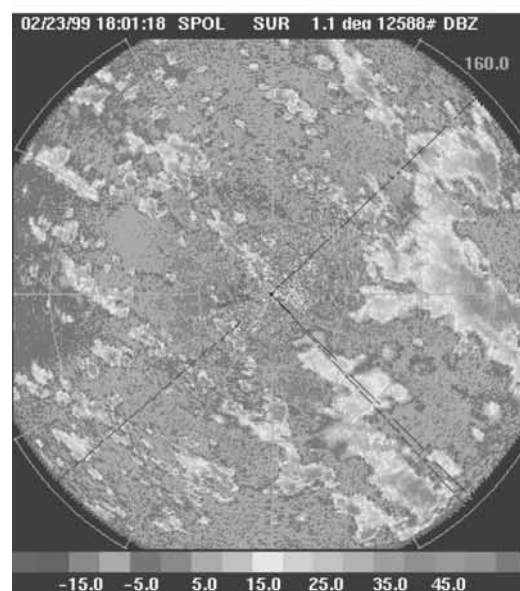
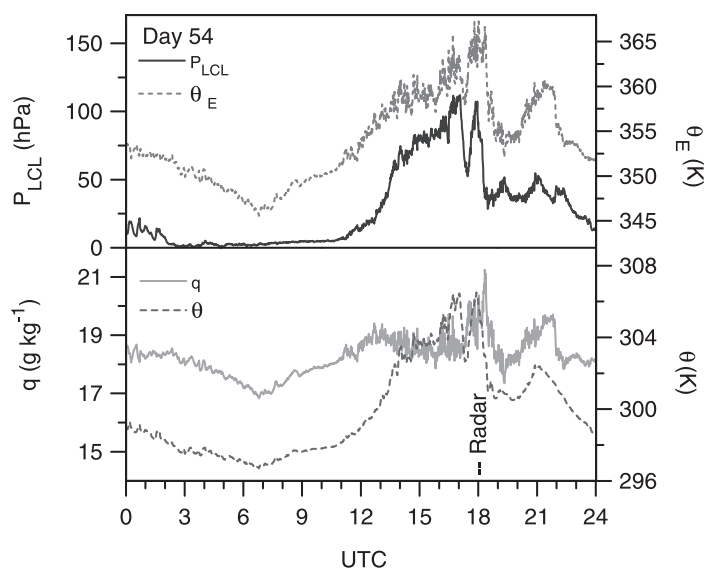
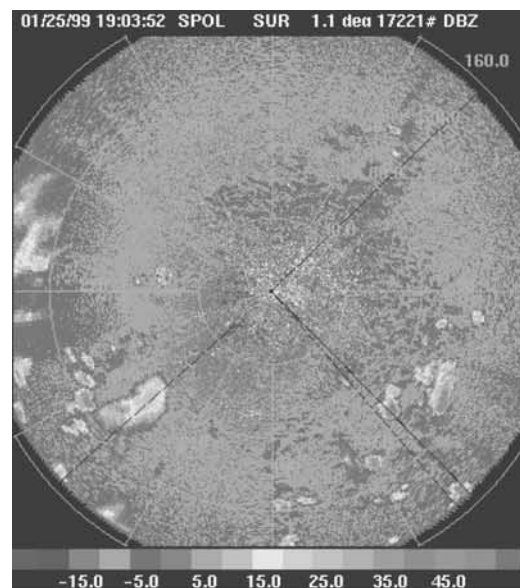
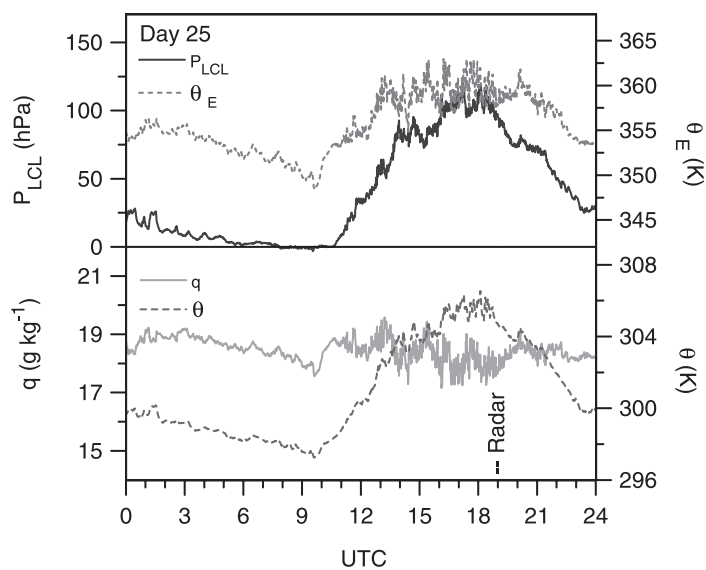
Rondônia pasture site) and an afternoon convective band group, which includes days from both regimes.

#### 3.1. Less Disturbed Days

[15] Figure 1 (top) shows an example of the diurnal cycle of  $\theta$ ,  $q$ ,  $\theta_E$ , and  $P_{LCL}$  (left) on 25 January, a day with little deep convection. On the right is an S-Pol radar scan at 1903 UTC, 1503 LST, which shows only small widely scattered convective cells, none of which are close to our pasture site observations, located north-west of the S-Pol radar on a bearing of  $323^\circ$  and at a range of 64 km (the maximum radar range shown is 150 km). The time of this afternoon radar scan is marked on the left-hand plot. On this day, temperature and potential temperature ( $\theta$ ) and the pressure height to the lifting condensation level ( $P_{LCL}$ ) (which is cloud base, as soon as shallow cumulus form) start rising about 1030 UTC (0630 LST) to a midafternoon maximum. After sunrise, mixing ratio ( $q$ ) first rises smoothly to about  $19 \text{ g kg}^{-1}$ , as surface evaporation is trapped in a relatively shallow stable layer. An hour or two after sunrise, a mixed boundary layer starts to deepen from the surface, capped by shallow cumulus, and from midmorning, there is a steady fall of mixing ratio with considerable fluctuations to a minimum of around  $17.5 \text{ g kg}^{-1}$  at 1800 UTC (1400 LST), the time of the surface temperature maximum. This is because the upward transport of water vapor out of the mixed layer (ML) into the cumulus cloud field must exceed the large surface evaporation (see section 3.4.2 later). After first rising from a minimum at sunrise, equivalent potential temperature ( $\theta_E$ ) fluctuates only about  $\pm 2 \text{ K}$  about 360 K, as ML  $\theta_E$  is controlled quite closely by the upward transport of warm moist air from the surface into shallow cumulus clouds. ML  $\theta_E$  is readily controlled by the shallow cloud field in the tropics, because in the rainy season the lower troposphere (up to the freezing level) is very unstable to moist processes. This quasi-equilibrium in  $\theta_E$  as  $\theta$  rises implies a fall of  $q$ , and in addition this rise of  $\theta$  and fall of  $q$  implies rising LCL. After the surface temperature maximum,  $\theta$  falls from 1800 to 2000 UTC, while  $q$  starts to rise again, maintaining the same  $\theta_E$ .

[16] The growth of the morning ML can be understood from Figure 2, which shows the predawn stable BL structure. The heavy line is an average of the two pairs of ascent and descent  $\theta$  profiles from the tethersonde at about 0630 and 0900 UTC, and the light line is the average of the two radiosondes launched at 0606 and 0845 UTC. The  $\theta$  profiles from the two sonde systems agree well. (The radiosonde mixing ratio is about  $1.5 \text{ g kg}^{-1}$  moister than the tethersonde below 900 hPa, not shown). To give insight into the formation of the nocturnal BL structure, the reference wet adiabat of 360 K is shown, which intersects a dry adiabat of  $\theta = 304 \text{ K}$  near 900 mb. These two are representative of the daytime ML dry adiabat, and the moist adiabat for ascent in the previous day's deep convection. Showers and down-drafts the previous day have transformed the lower troposphere from 940 to 800 hPa into one which is between the wet adiabat and dry adiabat in stability. This is typical of the transformation of the atmosphere by deep convection over land, both in the tropics and midlatitudes in summer [Betts,

**Figure 1.** (opposite) (Top) Diurnal cycle of  $\theta$ ,  $q$ ,  $\theta_E$ , and  $P_{LCL}$  on DOY = 25 (left) and (right) S-Pol radar scan at 1903 UTC (1503 LST). (Middle) As top for DOY = 54 with S-Pol radar scan at 1801 UTC (1401 LST). (Bottom) As top for DOY = 44 and S-Pol radar scan at 1807 UTC (1407 LST). See color version of this figure at back of this issue.



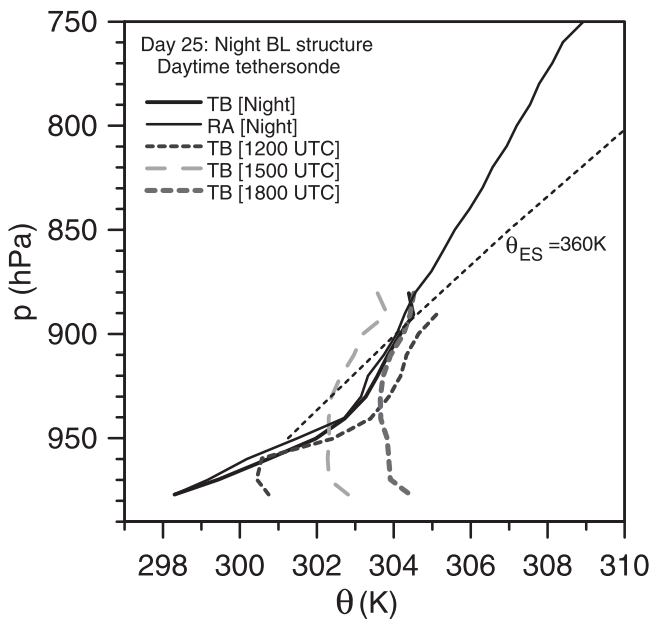


**Figure 2.** BL  $\theta$  structure from tethersonde (TB) and radiosonde (RA) on DOY = 25.

1976a, 1984]. The layer below 940hPa is much more stable than the wet adiabat, probably because it has been cooled more strongly at night by radiative processes and a small downward flux at the surface. The  $\theta_{ES}$  maximum of 364 K occurs at 940 hPa. This nocturnal BL has a subsaturated structure with an RH averaging about 85%, corresponding to a  $P_{LCL}$  of 35 hPa (not shown).

[17] After sunrise in the morning, when surface  $\theta = 297$  K, a mixed layer grows from the surface. A sequence of mean BL profiles from the tethersonde are shown. At 1200 UTC (0800 LST), the ML is still very shallow, trapped below the strongly stable layer. Mixing ratio at the surface at this time is  $19.1 \text{ g kg}^{-1}$  (Figure 1, top) since the surface evaporation is also trapped in this shallow layer. The tethersonde ascents at 1500 and 1800 UTC show the warming and deepening of the ML. Although there is some variability between sondes (note the variability at the surface in Figure 1), and entrainment at the ML-top speeds the process, it is clear that the ML can only deepen more rapidly once its potential temperature reaches about 303 K in midmorning, and its depth has reached the  $\theta_{ES}$  maximum at 940 hPa. This general pattern is seen on other days also (see composite in Figure 5 later), and while any single day is not in itself convincing, it seems that the fall of ML mixing ratio follows the more rapid deepening of the ML, and is linked to the vapor transport into the cloud field as discussed above. This pattern of double maxima in mixing ratio in the morning and again in the evening is typical of the diurnal cycle over land. It has been known for a long time [Geiger, 1965], and has been repeatedly seen in mean diurnal cycle data from field programs over land, including grasslands in Kansas [Betts and Ball, 1995] and the Canadian boreal forest [Betts et al., 2001].

### 3.2. Days With Frequent Scattered Showers

[18] Our second example is from the westerly regime in late February, with frequent showers from short-lived bands

of relatively shallow precipitating convection, as seen in the radar image for 1801 UTC (1401 LST) for 23 February (DOY 54): the middle panel of Figure 1. Starting around local noon the surface diurnal cycle is punctuated by showers, which modify the ML by evaporative cooling and moistening. On this day,  $\theta_E$  rises as high as 365 K, until it is sharply reduced around 1800 UTC as low  $\theta_E$  air is brought down to the surface from higher levels in a downdraft.

[19] Figure 3 shows the BL development on this day from a sequence of tethersondes (a mean of ascent and descent) and three radiosondes. The dotted line is  $\theta_{ES} = 352$  K, which shows that the early morning profile of temperature on this day was nearly wet adiabatic (contrast Figure 2). Indeed the low level structure was close to saturation for the first two hours after sunrise (Figure 1, middle, for the surface), and the surface net radiation (not shown) was low because of low cloud cover. The ML developed steadily (interrupted by weak showers) till a shower band passed over the site, shortly after 1800 UTC. There is no tethersonde data after that time, but the next radiosonde shows the stabilization of BL by the evaporation of rain and the development of a shallower ML.

### 3.3. Days With Major Convective System Passage Over the Pasture Site

[20] Our third example is 13 February (DOY 44), when a mesoscale convective band traveling from the north-east, shown in Figure 1 (bottom right) passed over the site in the afternoon. Figure 1 (bottom left) shows that on this day temperature rises until the line passage, and  $q$  falls slightly (with fluctuations), so that  $\theta_E$  climbs to values near 365 K just ahead of the line. As the strong cold downdraft from this system reaches the site,  $\theta$  falls about 7 K, and  $\theta_E$  falls more than 10 K. Figure 4 shows the  $\theta$  and  $\theta_E$  profiles from a sequence of tethersondes on this day, as well as two radiosondes. Figure 4 (top panel) shows the warming and growth

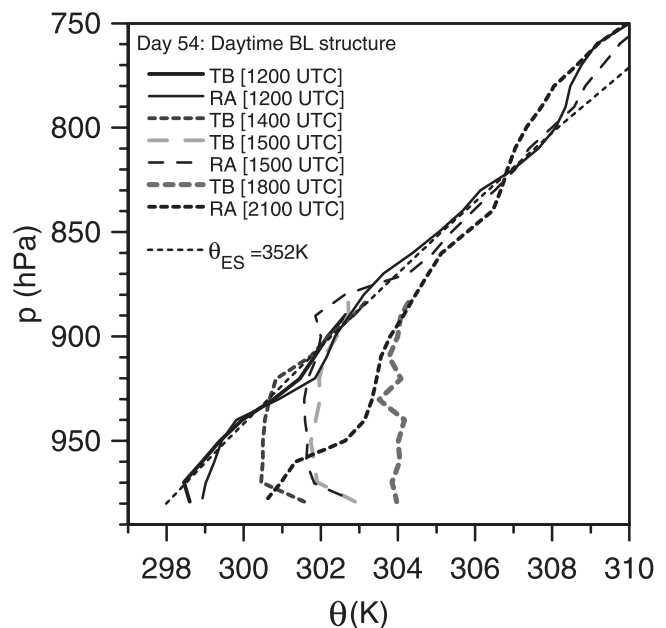


**Figure 3.** Daytime BL  $\theta$  structure from tethersonde and radiosonde on DOY = 54.



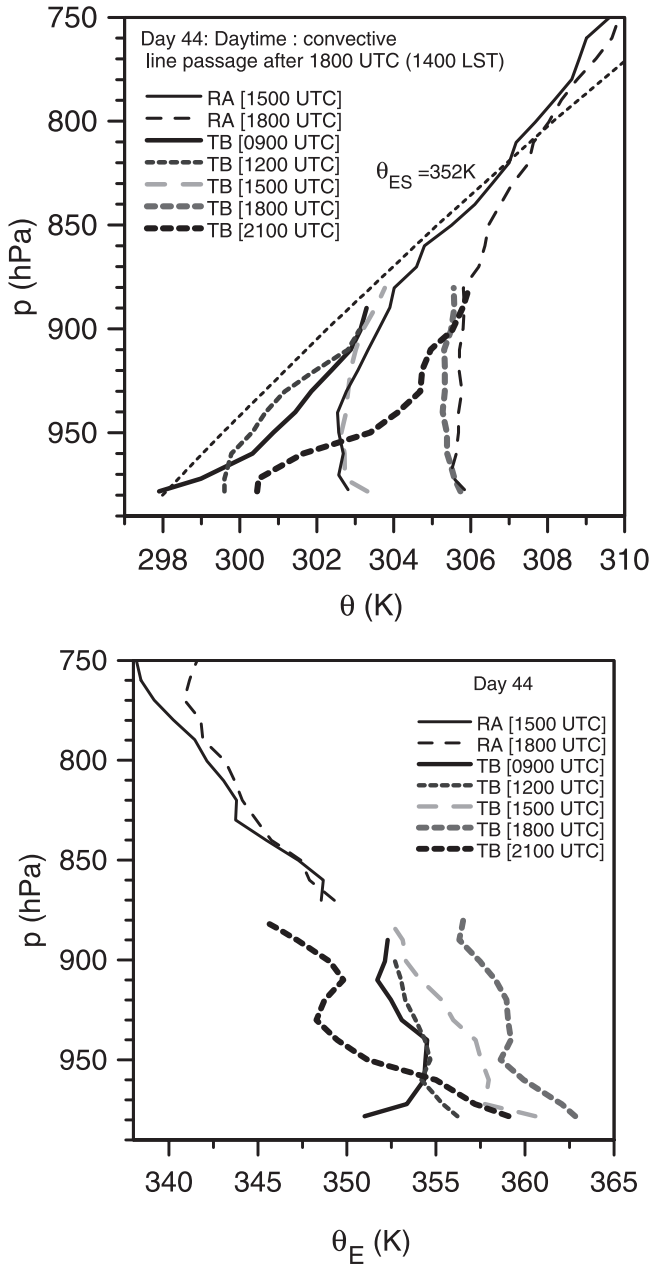


**Figure 4.** Daytime BL  $\theta$  structure (top) and  $\theta_E$  structure (bottom) from tethersonde and radiosonde on DOY = 44.

of the ML up to 1800 UTC, which is just before the passage of the convective line at this site, and a strong cooling below 900 hPa at 2100 UTC, the time of the next tethersonde. The bottom panel shows that  $\theta_E$  increases during the day up to 1800 UTC, and then falls sharply by about 10 K after the line passage. Note that at the surface (Figure 1, bottom),  $\theta_E$  falls as low as 352 K at the time of the line passage, but has recovered by 2100 UTC. The  $\theta_E$  profiles from the radiosondes are not shown from the surface to 870 hPa, because the humidity measurement from these sondes are less reliable than the tethersonde, especially just off the surface.

### 3.4. Diurnal Cycle Composites

[21] Composites are useful as they average over several days and the individual small scale convective events within

them, and give a picture of the mean diurnal cycle, more representative perhaps of the  $50 \times 50$  km grid square used in global forecast models. We examined the diurnal cycle for the 40 days (from DOY 20–59) for which we have data at the site, and put them in the five groups, shown in Table 3. The first four correspond to the surface easterly and westerly regimes, E2, W2, E3, and W3 [see Table 2: we have no data for the first 2 classes, E1 and W1]. The fifth is a composite of eight selected days, when a strong rainband passed directly over the measurement site in the midafternoon. We show this as a separate group, since strong convective downdrafts in the afternoon produce such a distinct modification to the diurnal cycle. The last column shows a mean daily precipitation, defined by first taking the mean of the rain gages in four networks, and then averaging these four means. These four networks, which were established to help calibrate the TRMM radars, are in a north-west to south-east line east of the pasture site [Negri *et al.*, 2002]. The two closest are network #2, which is about 25 km to the east and network #3 about 20 km to the north of the pasture site. Our basic grouping by the sequence of lower tropospheric easterly and westerly components also represents a time progression of the rainy season. Of the days in the afternoon rainband composite there are three (DOY 30, 31, and 38), when the lower tropospheric wind is from the north-north-west, but this was too small a sample to make a separate class.

#### 3.4.1. Surface Thermodynamic Cycle, Net Radiation, and Precipitation

[22] Figure 5 shows for the five composite plots of  $\theta$ ,  $q$ ,  $\theta_E$ , and  $P_{LCL}$ , incoming solar radiation (SolDn) and precipitation (derived from the average of four rain gage networks, as discussed above). The first composite (solid black) for the easterly surface flow in late January (East 20–28), represents a less disturbed daytime regime. Figure 1 (top) showed an example of one of these days. This composite has the warmest mean temperature, highest incoming solar radiation (associated with the least morning cloud cover), and the lowest mean precipitation. It also has the lowest mean mixing ratio and highest mean LCL. After sunrise,  $q$  rises sharply till 1130 UTC (0830 LST) as evaporation is trapped in the stable BL, then more slowly, peaks at about 1430 UTC (1030 LST) and then falls steadily during the daytime hours to a minimum in midafternoon. This daytime fall of  $q$  implies that water vapor is being transported out of the ML by convective clouds, faster than it is supplied by evaporation at the surface (see next section). After sunrise,  $\theta_E$  also rises sharply as the ML warms and moistens and then plateaus from 1600 to 1900 UTC with a value of 358–359 K. Precipitation in this composite peaks in the late afternoon.

[23] The second composite (solid gray) for the late January/early February westerly regime differs from the first primarily in that there is less morning SolDn (more morning cloud cover), so that temperature, LCL and  $\theta_E$  all rise less steeply to lower noon time values. There is less variation in  $q$  during the day, which is a little higher in the mean than the E2 composite, perhaps because mean daily precipitation is a little higher (see Table 2). There are three days in this group of ten when a convective band passed the site near 1800 UTC, and the impact of their downdrafts can be seen in the composite.

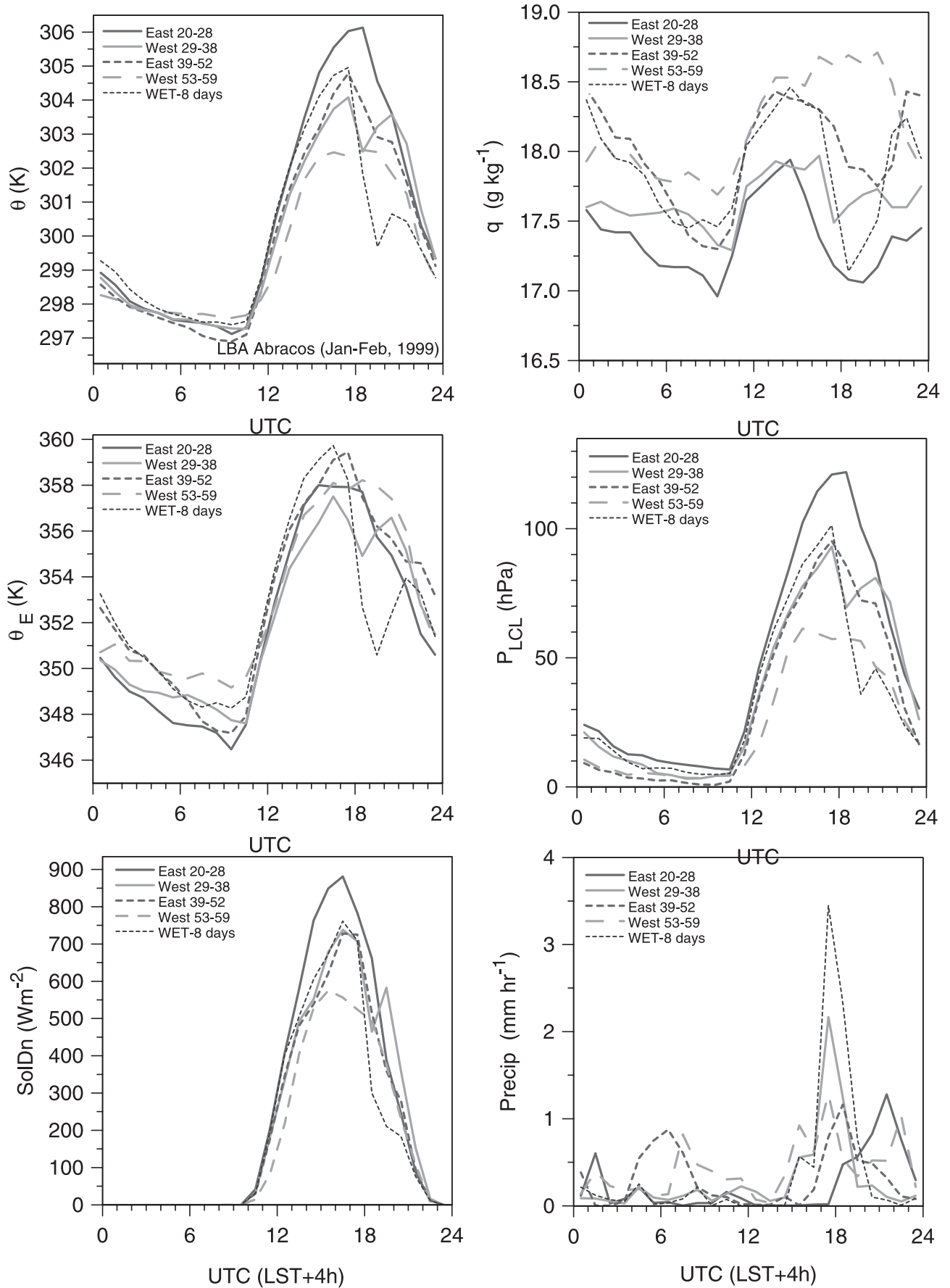


**Figure 5.** LBA Abracos composites by wind regimes and afternoon precipitation events.



[24] The third composite (black dashed) for the easterly regime in February (East 39–52) is similar to the first easterly composite, but  $\text{SolDn}$  is less (cloud cover is greater, following nighttime precipitation), so that mean temperature and LCL are reduced. The diurnal cycle of  $q$  is similar to the E2 regime, with a marked daytime drop of  $q$  after a midmorning maximum, although the mean is moister, perhaps because there are more showers in February, which increase BL  $q$  by evaporation. DOY 44 (Figure 1, bottom) was one of these days.

[25] This progression continues with the fourth composite (dashed gray) for the westerly regime at the end of February. These days are characterized by extensive but relatively shallow bands of showers. DOY 54 (Figure 1, middle) showed an example of one of these days. This composite is markedly cooler and moister in the daytime, with a lower LCL peaking at only 60 hPa, and there is no fall of mixing ratio during the daytime. However, afternoon  $\theta_E$  still reaches a similar mean value of 358 K. The daytime rise of  $\theta_E$  is limited by the upward advection of water vapor into non-precipitating and precipitating cumulus into a conditionally unstable atmosphere above, and the introduction of low  $\theta_E$  into the ML from downdrafts driven by evaporative cooling and condensate loading. Precipitation is greatest for this composite (consistent with the highest mixing ratio): it occurs both at night and in the day and starts by 1430 UTC in the late morning, lasting throughout the daytime period.

[26] This sequence of four composites shows a distinct progression toward a cooler, moister, shallower subcloud layer (with little change in maximum  $\theta_E$ ) with an increase in mean precipitation as the rainy season progresses. The easterly regime composites, but not the westerly composites, both show a daytime fall of  $q$  from 1400 to 2000 UTC. The WETAMC experiment was the beginning of long-term monitoring of the surface diurnal cycle and the surface fluxes at this pasture site. These data (which will be reported elsewhere), show the slow transition in the six months following the rainy season back to the much warmer, drier and deeper daytime BL, characteristic of the dry season in August [Nobre *et al.*, 1996].

[27] The final and distinct composite (black dotted) for the 8 days with the afternoon passage of a rainband over the site shows the impact of precipitation-driven downdrafts, which bring down cool, dry, low  $\theta_E$  air into the BL.  $\theta_E$  falls nearly 10 K at the surface with the arrival of this downdraft air. Precipitation peaks between 1700 and 1900 UTC. The afternoon rainband passage shown in Figure 1 (bottom) was also included in this group. We will explore the structure before and after downdraft passages at the site in more detail in section 3.5.

### 3.4.2. Surface Sensible Latent and Ground Heat Fluxes

[28] The surface energy balance can be written

$$R_N = H + LE + G + \text{residual} \quad (2)$$

where  $R_N$  is the net radiation,  $H$ ,  $LE$ , and  $G$  are the measured sensible, latent, and ground heat fluxes. Measurement errors leave a small residual, which for a daily average is about 4% of the daily mean  $R_N$ , and about 5% for corresponding daytime averages. Figure 6 shows the five composites for the same groups of days in Table 3

(except for the last westerly group (W3) for which we only have flux data for the three days 54–56), with the surface sensible and latent heat fluxes in the upper panels, and the ground heat flux and Bowen ratio (lower panels). The Bowen ratio,  $BR$ , plotted for the daytime period only, is defined as

$$BR = H/LE \quad (3)$$

The upper panels for  $H$  and  $LE$  are similar, following the pattern of  $\text{SolDn}$  in Figure 5. The Bowen ratio, shown in the lower right panel, is relatively flat during the daytime, with  $H \approx 0.4LE$ . Fluxes are highest for the earliest easterly composite and lowest for the last westerly composite. The ground heat flux,  $G$ , has a similar pattern. The dotted curve dips below zero in the afternoon for the convective band composite, consistent with the sharp fall of temperature in Figure 5. The differences in  $BR$  are more subtle. The earlier and drier composites have a slightly higher  $BR$  than the two later composites and the afternoon rainband composite (all of which have higher rainfall).

[29] Note that the last westerly composite with the lowest fluxes ( $\text{SolDn}$ ,  $H$  and  $LE$ ) also has the highest mean daytime mixing ratio. Thus, we see again that it is not the surface evaporation that is alone responsible for the BL equilibrium of  $q$ , but also the interaction with the cloud layer. In this case surface evaporation is lowest, but the subcloud layer is the shallowest, since the evaporation of falling rain from many weak downdrafts is maintaining a cooler moister subcloud layer.

[30] Figure 7 plots daytime (0600–1800 LST) averages against the mean date of each composite. For the time period we have data, there is a systematic downward trend of the mean fluxes, as the rainy season progresses, and mean  $BR$  also falls from the beginning to the end of the period. The average fluxes for the rainband “WET-8” composite, which are selected days from the entire period, are plotted as the symbol W.

## 3.5. Rainband Passage Composites

[31] One of the composites in Figures 4–6 was that for 8 days when a convective rainband passed in early afternoon. We can enlarge the sample by including all the rainband passages between 1730 and 2200 UTC and still depict the sharp transition by compositing centered on the arrival time of the cold gust front. There are 18 well-defined events (all from different days: DOY = 20, 22, 23, 24, 26, 29, 30, 31, 38, 40, 42, 44, 48, 50, 51, 54, 55, and 56) during the period we have data. Of these, 11 are in the easterly wind regimes and 7 in the westerly regimes, so we composite them separately.

### 3.5.1. Surface Downdraft Composite

[32] Figure 8 shows the surface transformation from a westerly composite (7 downdraft events) and the easterly composite (11 downdraft events) plotted on conserved variable diagrams for ( $\theta_E$ ,  $P_{LCL}$ ), and ( $q$ ,  $\theta$ ). The composites were constructed by selecting 3 hours of the surface data ahead and after the arrival of the sharp temperature fall marking the passage of a surface gust front. The one minute micromet data has been averaged into sequential 10-min blocks, so that blocks 1–18 (numbered on Figure 8) are ahead of the gust front, with time block = 18 being the

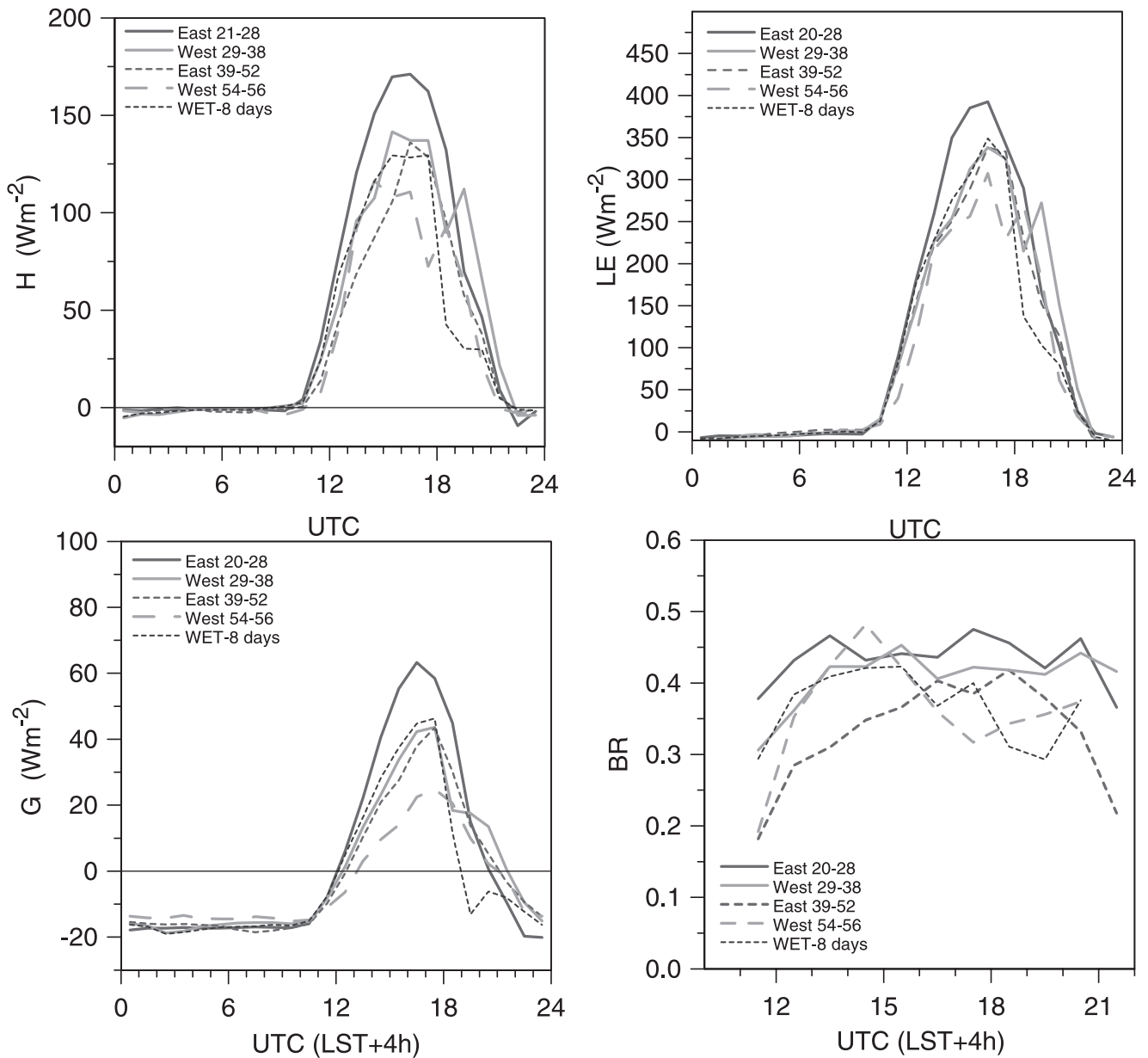


**Figure 6.** Composite diurnal cycle of  $H$ ,  $LE$  (upper panels);  $G$  and Bowen ratio (lower panels).

10 min just before the sharp fall of surface temperature. The average end-time corresponding to point 18 is 1859 UTC for the easterly composite and 1927 UTC for the westerly one. The figure shows that the fall of  $\theta$ ,  $q$ ,  $\theta_E$ , and  $P_{LCL}$  at the surface lasts on average 30 min. For the easterly composite, conditions ahead of the gust front arrival are warmer and drier with a higher cloud base, than for the westerly composite.

Conditions in the cold outflow air are much more similar for both, with the result that while the fall of  $\theta_E$  is about  $-10$  K for both,  $P_{LCL}$  falls by  $-70$  hPa for the easterly composite, but only  $-50$  hPa for the westerly one. Similarly,  $\theta$  falls more for the easterly composite (about  $-6$  K versus  $-5$  K) while  $q$  falls a little less (about  $-0.9$  versus  $-1.3$  g kg $^{-1}$ ). Composites such as these are useful reference points,

**Table 3.** Surface Diurnal Composites

Composite Name	Days Included, UTC	No. of Days	Mean Daily Precipitation, mm
1. East 20–28 (E2)	20–28	9	5.67
2. West 29–38 (W2)	29–38	10	6.94
3. East 39–52 (E3)	39–52	14	7.48
4. West 53–59 (W3)	53–59	7	10.14
5. WET-8 days	20, 24, 30, 31, 38, 42, 44, 48 (afternoon rainband)	8	8.94

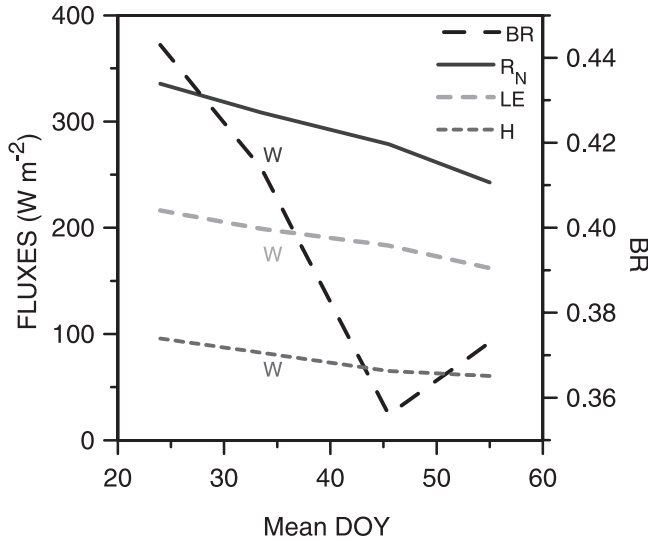


**Figure 7.** Trend of daytime average fluxes and Bowen ratio (right-hand-scale) during rainy season.

because one of the key problems in convective parameterization for the tropics is the incorporation and proper calibration of convective downdraft models. Although the sample size for the westerly wind composite is a little small to be satisfactory, the picture is consistent with the westerly wind days having more frequent showers and a lower mean cloud base. The tethersonde data in the next section gives a consistent vertical picture.

### 3.5.2. BL Composite of Rainband Passage

[33] For 13 of these 18 events, we have tethersonde profiles before and after the convective system passed over the site in the afternoon. Figure 9 shows the change in the composite thermodynamic structure, associated with the convective band passage, again separated into easterly (7 events: mean gust front arrival time 1920 UTC (1520 LST) and westerly wind regimes (6 events: mean time 1903 UTC (1503 LST)). The upper panel shows the mean drop of  $q$ , as downdrafts bring down drier air, and the middle panel the cooling and stabilization of the BL. These two show, consistent with Figure 8, that the inflow air for the westerly regime is cooler and moister, but they also show that air on the outflow side has somewhat similar properties for both easterly and westerly regimes. Because the mean time interval (see middle panel legend) between these mean tethersonde profiles is 5–6 hours (the “after” profile is on average 3–4 hours after the arrival of the gust front), some modification at the surface can be expected. Figure 8 shows  $1 \text{ g kg}^{-1}$  of moistening in the three hours after line passage. The LCL of surface air in the “before” composites is shown in the middle panel. The layer that has been thermally cooled appears to be a little deeper than the subcloud layer, which is shallower for the westerly regime. The bottom panel shows on the left that the fall of  $\theta_E$  is about 6 K for both composites throughout the whole layer, and extends above 900 hPa. On the right (with the label S) are the profiles of  $\theta_{ES}$ , corresponding to the middle panel. Together the  $\theta$  and  $\theta_{ES}$  profiles show that the thermal transformation near the surface is from approximately constant  $\theta$  to approximately constant  $\theta_{ES}$ . This BL

transformation is very similar to that seen over Venezuela and the Great Plains of the United States in summer [Betts, 1976a, 1984], and for convective lines in the tropical Atlantic [Barnes and Sieckman, 1984].

### 3.5.3. Gust Front Transition

[34] A number of the tethersonde profiles at 1800 UTC (1400 LST), a standard radiosonde launch time, were just ahead of the arrival of a convective band, so that the ascent was in the inflow air, but the descent caught the initial arrival of the gust front. Figure 10 shows an average of three cases on DOY = 38, 40, and 48. The heavy solid curve (with a mean time of 1745 UTC) is just ahead of the arrival of the gust front, showing a subcloud layer with  $\theta \approx 304 \text{ K}$  (middle panel) and a wind speed, nearly constant in the vertical, of  $3 \text{ m s}^{-1}$  (top-left). The ascents reach only 920 hPa, as they were terminated early with the approach of the gust-front. The mean descent sounding enters the cooled gust-front air at 1800 UTC, with wind speeds approaching

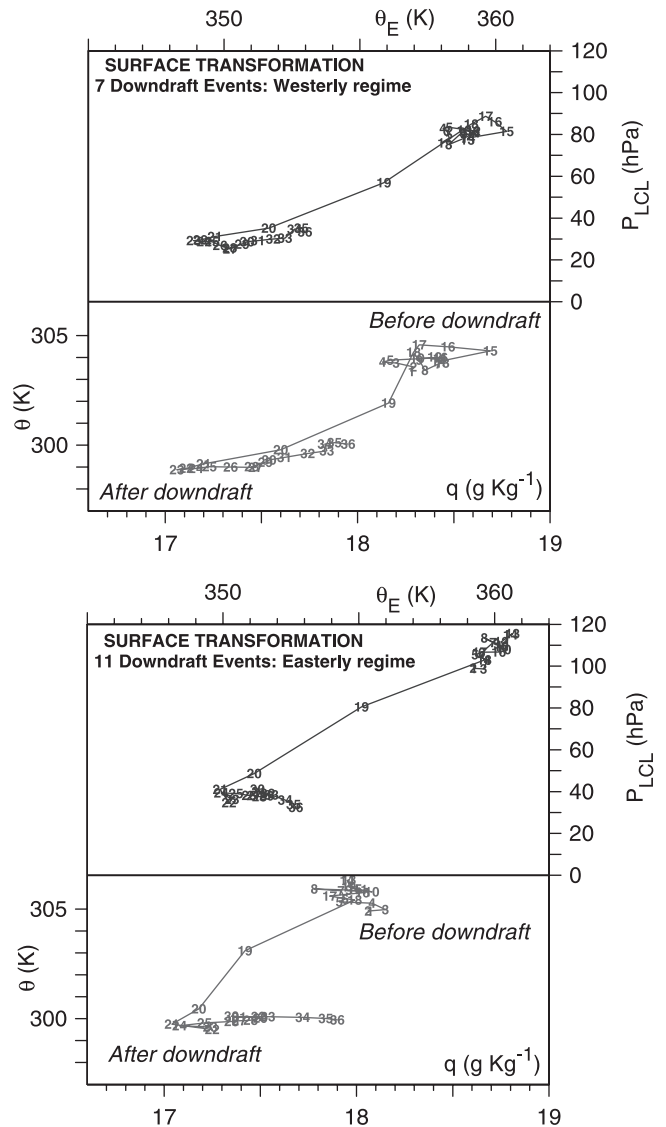


**Figure 8.** Composite of surface passage of 7 downdraft events in westerly regime (upper) and 11 events in easterly regime (lower).



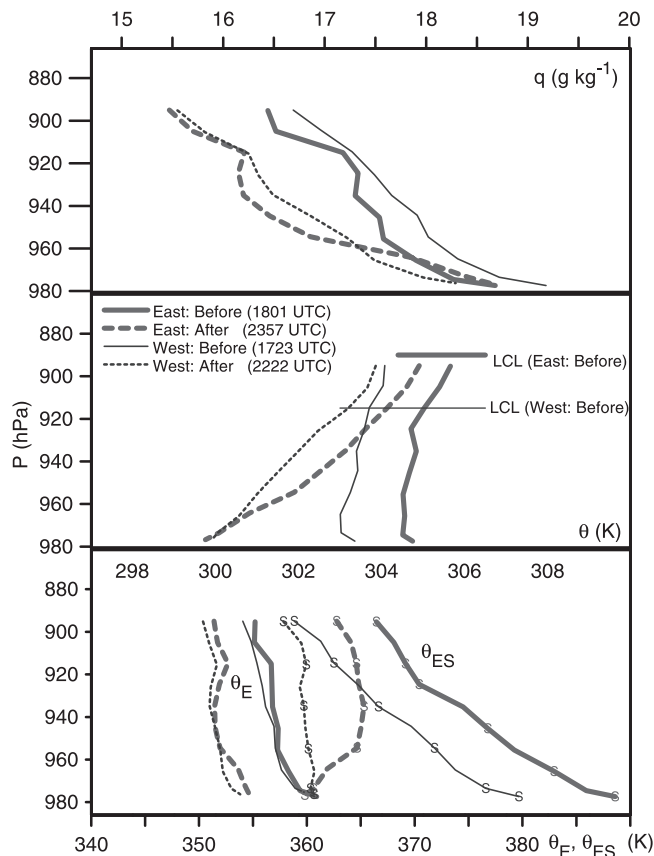


**Figure 9.** Composite BL profiles before and after the passage of 13 convective systems.

10 m s<sup>-1</sup>. Note however, that initially the cooled air is moister with the same  $\theta_E = 358$  K, indicating subcloud layer air that has been cooled evaporatively. In fact, the tetheredsonde only encounters lower  $\theta_E$  air as it approaches the surface. On these three days, the surface  $\theta_E$  dropped to a mean minimum of 351.5 K by 1820 UTC. The tetheredsonde profiles nearly four hours later at 2155 UTC (heavy dashes) show the typical cooler drier, stable outflow air profile with lower  $\theta_E$  and a nearly constant wet adiabatic structure with  $\theta_{ES} \approx 363$  K.

[35] This transition in the structure of outflow air has been noticed in earlier studies [e.g., Betts, 1984]. Recently Tompkins [2001], from a numerical simulation, has drawn attention to the fact that the triggering of new convection by cold pool outflows over the ocean appears to involve the lifting of this cooled but high  $\theta_E$  air. However, land and sea respond differently to a downdraft event. Over the ocean, the surface heat flux rapidly restores the temperature, while over land, evaporation during the daylight hours increases mixing ratio and  $\theta_E$ , rather than temperature, as shown in Figure 9. Both processes though could lead to higher  $\theta_E$  air along gust front boundaries, where the initial evaporative modification conserves  $\theta_E$  in subcloud layer air.

#### 4. Summary and Conclusions

[36] We have discussed the surface diurnal cycles of temperature, humidity, lifting condensation level, equivalent potential temperature, and the surface fluxes, for easterly

and westerly lower tropospheric wind regimes in Rondônia during the LBA wet season experiment of January and February of 1999, using data collected in support of the ground validation for TRMM. This is an important data set, as it is one of the first over land in the tropics, where simultaneous observations were intercompared at the surface, from tethered balloons within the boundary layer and from rawinsonde ascents through the troposphere. This analysis raises several important issues for modeling the land-surface-atmosphere interaction in the tropics. We have shown examples of different convective regimes seen during easterly and westerly flows in the lower troposphere, and discussed some of the differences in structure they exhibited. We then composited surface and tetheredsonde databased on these wind regimes. The easterly diurnal composites show a characteristic early morning maximum of  $q$ , followed by a fall to a minimum in the late afternoon, as cumulus clouds mix water vapor up and out of the subcloud layer, keeping  $\theta_E$  close to a mean value of 358 K. There is a steady transition during the rainy season toward cloudier conditions, lower surface fluxes and a slightly lower Bowen ratio (although the rainy season daytime surface Bowen ratio remains close to 0.4 at this pasture site). Composites of the surface and BL transitions associated with the passage of convective bands, show the characteristic properties of convective downdraft air for the different wind regimes. Typically  $\theta_E$  falls by about

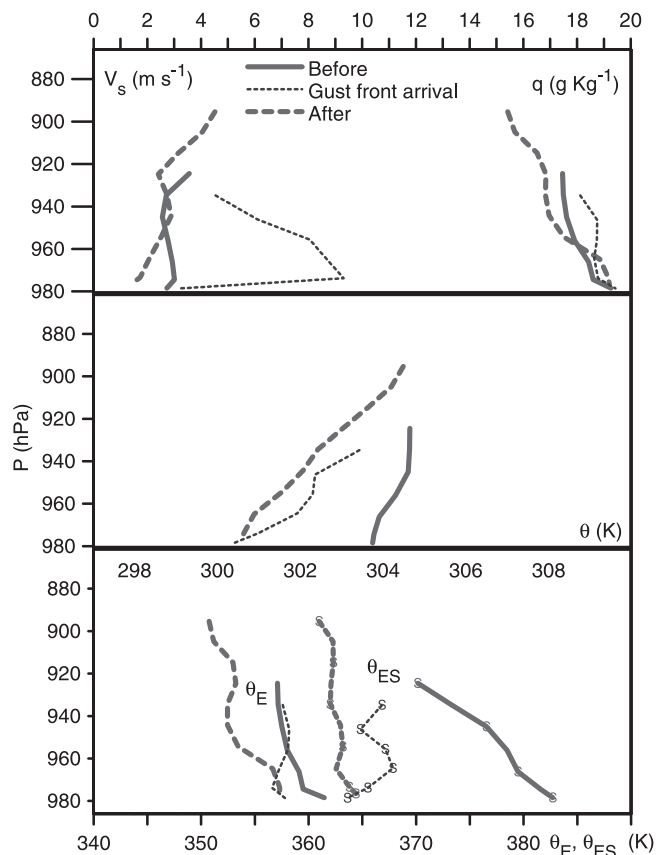


**Figure 10.** Composite BL profiles ahead of, through gust front and after convective lines.

10 K at the surface and  $\theta$  by 4–5 K. The layer of cooling corresponds roughly to the transformation of the subcloud layer from a dry to wet adiabatic structure, consistent with earlier studies. However, the layer in which  $\theta_E$  is reduced by downdrafts appears to extend above the first 100 hPa reached by the tether sondes. Since the mean cloud base is lower for the westerly regime composite, the layer of cooling is shallower for this group (and probably downdraft intensity is also). The shallower cloud base (that is a cooler, moister subcloud layer) is in itself probably caused by the evaporation in downdrafts from more frequent transient systems, so that a different diurnal cycle of  $\theta$  and  $q$  results. Tether sonde ascents through the edges of gust fronts show that subcloud air is first cooled and moistened by rainfall evaporation, before the arrival at the surface of lower  $\theta_E$  air from higher levels.

[37] Our analysis is quite limited in scope and addresses the thermodynamic structure in only the lowest 100 hPa. We have not examined the detailed kinematic structure of the different regimes in Rondônia. Several case studies of the structure mesoscale systems are included in this special issue [Cifelli *et al.*, 2002; Silva Dias *et al.*, 2002b], and comparisons need to be made with convective systems from other regions such as the tropical Pacific [LeMone *et al.*, 1998; Lewis *et al.*, 1998]. Modeling studies in progress on different scales are providing sharply contrasting results. Nested nonhydrostatic models resolving down to a few kilometers show the triggering of new convective cells from cold downdraft outflows [Silva Dias *et al.*, 2002b], but appear over Amazonia to overpredict development and precipitation (P. Silva Dias, personal communication, 2001). A companion paper [Betts and Jakob, 2002] shows that the onset of precipitation in the ECMWF forecast model is much too early in the diurnal cycle, because the morning development of the shallow cumulus layer is not properly represented. The model also does not represent the diurnal cycle differences between the easterly and westerly regimes over Rondônia. As in many forecast models, shallow and deep cumulus convection are parameterized separately in the ECMWF model, but it is clear from this LBA data that they are closely intertwined in their impacts on the daytime evolution of the ML, particularly during the westerly regime at the end of February. In addition, most parameterization schemes for precipitating convection in large-scale models do not properly account at present for the different dynamical and microphysical structure of the convective bands in different wind regimes. The Rondônia wet season data will provide a further observational basis for model development, but further synthesis will be needed. Our thermodynamic composites show small differences in the diurnal cycle: a trend toward a cooler moister BL as the rainy season progresses, and a weaker diurnal cycle of mixing ratio in the westerly regime. In our tether sonde composites it appears that the differences in cloud base are associated with differences in downdraft intensity, frequency and structure, but in such a tightly coupled system in which the subcloud structure is strongly influenced by evaporation from the more frequent transient convection bands in the westerly regime, cause and effect are not fully clear.

## Appendix A: Thermodynamic Formulae

Variable	Formula used
p [hPa] pressure	[Measured]
T [°C] temperature	[Measured]
RH [fraction] relative humidity	[Measured]
$\theta$ [K] potential temperature	$(T + 273.15) * (1000/p)^{0.286}$
QS [g kg <sup>-1</sup> ] saturation mixing ratio	$622 / (0.16361 * p * \text{EXP}(-17.67 * T / (T + 243.5))) - 1$
q [g kg <sup>-1</sup> ] mixing ratio	$\text{RH} * \text{QS} / (1 + (\text{QS} / 622) * (1 - \text{RH}))$
T* [K]: LCL saturation temperature	$55 + (2840 / (3.5 * \text{LN}(\theta) - \text{LN}(1000 * q / (622 + q)))) - 4.805$
p* [hPa]: LCL saturation pressure	$1000 * (T^* / \theta)^{3.4965}$
P <sub>LCL</sub> [hPa]	$p^* - p$
$\theta_E$ [K] equiv. pot. temperature	$\theta * \text{EXP}(2.67 * q / T^*)$

[38] **Acknowledgments.** This LBA data collection was supported by a NASA-TRMM grant to the University of Virginia. Alan Betts is supported by NASA under grant NAG5-8364, and by NSF under Grant ATM-9988618. The S-Pol radar is operated by the Atmospheric Technology Division, National Center for Atmospheric Research, which is sponsored by the National Science Foundation. We are grateful to the reviewers for their careful reading of the text.

## References

- Barnes, M., and K. Sieckman, The environment of fast- and slow-moving tropical convective cloud lines, *Mon. Weather Rev.*, **112**, 1782–1794, 1984.
- Betts, A. K., The thermodynamic transformation of the tropical subcloud layer by precipitation and downdrafts, *J. Atmos. Sci.*, **33**, 1008–1020, 1976a.
- Betts, A. K., Modeling subcloud layer structure and interaction with shallow cumulus layer, *J. Atmos. Sci.*, **33**, 2363–2382, 1976b.
- Betts, A. K., Saturation point analysis of moist convective overturning, *J. Atmos. Sci.*, **39**, 1484–1505, 1982.
- Betts, A. K., Boundary layer thermodynamics of a High Plains severe storm, *Mon. Weather Rev.*, **112**, 2199–2211, 1984.
- Betts, A. K., FIFE atmospheric boundary layer budget methods, *J. Geophys. Res.*, **97**, 18,523–18,532, 1992.
- Betts, A. K., The parameterization of deep convection, in *The Physics and Parameterization of Moist Atmospheric Convection*, NATO ASI Ser. C, vol. 505, edited by R. K. Smith, chap. 10, pp. 255–279, Kluwer Acad., Norwell, Mass., 498 pp., 1997.
- Betts, A. K., Surface diurnal cycle over Venezuela, *Meteorol. Atmos. Phys.*, **67**, 213–216, 1998.
- Betts, A. K., and J. H. Ball, The FIFE surface diurnal cycle climate, *J. Geophys. Res.*, **100**, 25,679–25,693, 1995.
- Betts, A. K., and C. Jakob, Evaluation of the diurnal cycle of precipitation, surface thermodynamics and surface fluxes in the ECMWF model using LBA data, *J. Geophys. Res.*, **107**, 10.1029/2001JD000427, in press, 2002.
- Betts, A. K., and M. F. Silva Dias, Unsaturated downdraft thermodynamics in cumulonimbus, *J. Atmos. Sci.*, **36**, 1061–1071, 1979.
- Betts, A. K., J. H. Ball, and J. H. McCaughey, Near-surface climate in the boreal forest, *J. Geophys. Res.*, **106**, 33,529–33,542, 2001.
- Bolton, D., The computation of equivalent potential temperature, *Mon. Weather Rev.*, **108**, 1046–1053, 1980.
- Cifelli, R., W. A. Petersen, L. D. Carey, S. A. Rutledge, and M. A. F. Silva Dias, Radar observations of the kinematic, microphysical, and precipitation characteristics of two MCSs in TRMM-LBA, *J. Geophys. Res.*, **107**, 10.1029/2000JD000264, in press, 2002.
- Emanuel, K., *Atmospheric Convection*, 580 pp., Oxford Univ. Press, New York, 1994.
- Fitzgarrald, D. R., B. L. Stormwind, G. Fisch, and O. M. R. Cabral, Turbulent transport observed just above the Amazon forest, *J. Geophys. Res.*, **93**, 1551–1563, 1988.
- Garstang, M., and D. R. Fitzgarrald, *Observations of Surface to Atmosphere Interactions in the Tropics*, Oxford Univ. Press, New York, 405 pp., 1999.
- Geiger, R., *The Climate Near the Ground*, Harvard Univ. Press, Cambridge, Mass., 611 pp., 1965.

- Harris, R. C., et al., The Amazon Boundary-Layer Experiment (Able-2a) - Dry season 1985, *J. Geophys. Res.*, **93**, 1351–1360, 1988.
- Herdies, D. L., A. Da Silva, and M. A. F. Silva Dias, The bimodal pattern of the summer circulation over South America, *J. Geophys. Res.*, **107**, 10.1029/2001JD000997, in press, 2002.
- LeMone, A., J. Zipser, and B. Trier, The role of environmental shear and thermodynamic conditions in determining the structure and evolution of mesoscale convective systems during TOGA COARE, *J. Atmos. Sci.*, **23**, 3493–3518, 1998.
- Lewis, A., A. LeMone, and P. Jorgensen, Evolution and dynamics of a late-stage squall line on 20 February 1993 during TOGA COARE, *Mon. Weather Rev.*, **126**, 3189–3212, 1998.
- Mahrt, L., Mixed layer moisture structure, *Mon. Weather Rev.*, **104**, 1403–1407, 1976.
- Martin, C. L., D. Fitzgarrald, M. Garstang, A. P. Oliveira, S. Greco, and E. Browell, Structure and growth of the mixing layer over the Amazonian rain forest, *J. Geophys. Res.*, **93**, 1361–1375, 1988.
- Marengo, J., G. Fisch, I. Vendrame, P. Cervantes, and C. Morales, On the diurnal and day-to-day variability of rainfall in southwest Amazonia during the LBA-TRMM and LBA-WET AMC campaigns of summer 1999, *J. Geophys. Res.*, **107**, 10.1029/2001JD001188, in press, 2002.
- Negri, A. J., L. Xu, and R. F. Adler, A TRMM-calibrated infrared rainfall algorithm applied over Brazil, *J. Geophys. Res.*, **107**, 10.1029/2000JD000265, 2002.
- Nobre, C. A., G. Fisch, H. R. da Rocha, R. F. F. Lyra, E. P. da Rocha, and V. N. Ubarana, Observations of the atmospheric boundary layer in Rondônia, in *Amazonian Deforestation and Climate*, edited by J. H. C. Gash, C. A. Nobre, J. M. Roberts, and R. L. Victoria, John Wiley, New York, pp. 413–424, 1996.
- Pereira Filho, A. J., M. A. F. Silva Dias, R. I. Albrecht, L. G. P. Pereira, A. W. Gandu, O. Massambani, A. Tokay, and S. A. Rutledge, Multisensor analysis of a squall line in the Amazon region, *J. Geophys. Res.*, **107**, 10.1029/2001JD000305, in press, 2002.
- Peterson, W. A., S. W. Nesbitt, R. J. Blakeslee, R. Cifelli, P. Hein, and S. A. Rutledge, TRMM observations of intraseasonal variability in convective regimes over the Amazon, *J. Clim.*, **15**, 1278–1294, 2002.
- Rickenbach, T. M., R. N. Ferreira, J. Halverson, D. L. Herdies, and M. A. F. Silva Dias, Modulation of convection in the southwestern Amazon Basin by extratropical stationary fronts, *J. Geophys. Res.*, **107**, 10.1029/2001JD000263, in press, 2002.
- Riehl, H., *Climate and Weather in the Tropics*, Academic, San Diego, Calif., 609 pp., 1979.
- Rutledge, S. A., W. A. Petersen, R. C. Cifelli, and L. D. Carey, Early results from TRMM-LBA: Kinematic and microphysical characteristics of convection in distinct meteorological regimes, paper presented at AMS 24th Conference on Hurricanes and Tropical Meteorology, 29 May–2 June, 2000, Ft. Lauderdale, Fla. 2 pp., 2001.
- Silva Dias, M. F., and P. L. Silva Dias, Observed thermodynamic structure of the sub-tropical atmosphere in the presence of precipitation, paper presented at 1st Conference on Southern Hemisphere Meteorol., Sao José dos Campos, SP, Brazil, 1–5 August, 1983.
- Silva Dias, M. A. F., et al., Clouds and rain processes in a biosphere atmosphere interaction context in the Amazon Region, *J. Geophys. Res.*, **107**, 10.1029/2001JD000335, in press, 2002a.
- Silva Dias, M. A. F., et al., A case study of convective organization into precipitating lines in the Southwest Amazon during the WETAMC AND TRMM-LBA, *J. Geophys. Res.*, **107**, 10.1029/2001JD000375, in press, 2002b.
- Tao, W. K., J. Simpson, C. H. Sui, C. L. Shie, B. Zhou, K. M. Lau, and M. Moncrieff, Equilibrium states simulated by cloud-resolving models, *J. Atmos. Sci.*, **56**, 3128–3139, 1999.
- Tompkins, A. M., The organization of tropical convection in low vertical wind shears: The role of cold pools, *J. Atmos. Sci.*, **58**, 1650–1672, 2001.
- Zipser, E. J., The role of organized unsaturated convective downdrafts in the structure and rapid decay of an equatorial disturbance, *J. Appl. Meteorol.*, **8**, 799–814, 1969.

A. K. Betts and J. H. Ball, Atmospheric Research, 58 Hendee Lane, Pittsford, VT 05763, USA. (akbetts@aol.com)

J. D. Fuentes and M. Garstang, Department of Environmental Sciences, University of Virginia, Charlottesville, VA, USA.



---

**Figure 1.** (opposite) (Top) Diurnal cycle of  $\theta$ ,  $q$ ,  $\theta_E$ , and  $P_{LCL}$  on DOY = 25 (left) and (right) S-Pol radar scan at 1903 UTC (1503 LST). (Middle) As top for DOY = 54 with S-Pol radar scan at 1801 UTC (1401 LST). (Bottom) As top for DOY = 44 and S-Pol radar scan at 1807 UTC (1407 LST).

